

Multipolar fluctuations from localized 4f electrons in CeRh₂As₂

Koki Numa,¹ Eri Matsuda,¹ Akimitsu Kirikoshi,² and Junya Otsuki²

¹Department of Physics, Okayama University, Okayama 700-8530, Japan

²Research Institute for Interdisciplinary Science, Okayama University, Okayama 700-8530, Japan
(Dated: December 29, 2025)

The heavy-fermion superconductor CeRh₂As₂ exhibits a non-superconducting phase transition that precedes the emergence of superconductivity. The nature of the corresponding order parameter remains under debate, with competing proposals involving magnetic dipoles or electric quadrupoles. We derive the momentum-dependent multipolar susceptibilities and effective interactions among the localized 4f electrons, based on the framework of density functional theory combined with dynamical mean-field theory. Magnetic fluctuations within the crystalline-electric-field (CEF) ground-state doublet are dominated by $\mathbf{q} = (1/2, 1/2, 0)$, corresponding to a two-dimensional checkerboard configuration of the magnetic moment M_z along the c axis. Hybridization between the CEF ground state and the first-excited doublet gives rise to leading magnetic octupole fluctuations of $z(x^2 - y^2)$ symmetry, followed by electric quadrupole fluctuations of $x^2 - y^2$ and $\{yz, zx\}$ symmetries. By taking into account the anisotropic magnetic-field dependence of the transition temperature T_0 , we conclude that an antiferromagnetic order of M_z at $\mathbf{q} = (1/2, 1/2, 0)$ is consistent with the experiments, owing to the enhancement of T_0 caused by fluctuations of the field-induced quadrupole of $\{yz, zx\}$ type under an in-plane magnetic field.

I. INTRODUCTION

Cerium-based materials exhibit superconductivity, magnetism, and multipolar ordering. Their distinctive properties often originate from the large total angular momentum $j = 5/2$ arising from the strong spin-orbit coupling. The absence of local inversion symmetry can further give rise to exotic electronic states such as odd-parity order parameters. CeRh₂As₂ is one such material that has recently attracted considerable attention.

CeRh₂As₂ is a heavy-fermion superconductor with a critical temperature $T_{SC} \approx 0.3$ K and a large Sommerfeld coefficient of 700–1200 mJ/mol K² [1, 2]. Its crystal structure is of CaBe₂Ge₂-type, belonging to the non-symmorphic space group $P4/nmm$ (D_{4h}^7 , No. 129). This structure is closely related to the well-known ThCr₂Si₂-type structure in space group $I4/mmm$ (D_{4h}^{17} , No. 139), but lacks local inversion symmetry at the Ce site as illustrated in Fig. 1(a). A notable feature of this compound is that the superconducting state persists up to $H_{c2} \approx 14$ T for a magnetic field along the c axis, which is anomalously high relative to the energy scale of $T_{SC} \approx 0.3$ K [1]. The superconducting phase is divided by a first-order phase transition at $H \approx 3.9$ T into a low-field phase (SC1) and a high-field phase (SC2) [1–4], as schematically illustrated in Fig. 1(b). Moreover, antiferromagnetism coexists with the superconductivity in SC1 phase, as suggested by NQR [5] and muon spin relaxation (μ SR) [6]. The superconducting properties of this material have been extensively investigated through NMR/NQR [5, 7–10], optical conductivity [11], thermal conductivity [12], angle-resolved photoemission spectroscopy (ARPES) [13, 14], inelastic neutron scattering [15], an external pressure [16, 17], point contact spectroscopy [18], and electronic structure calculations [19–23]. Theoretical investigations address superconductivity influenced by, for example, the nonsymmorphic struc-

ture and the Rashba spin-orbit coupling caused by non-centrosymmetry of correlated sites [24–39].

Another intriguing property in CeRh₂As₂ is a non-superconducting phase transition at $T_0 \approx 0.5$ K, detected in specific heat, thermal expansion, and resistivity measurements [1, 2, 40, 41]. The phase in the range $T_{SC} < T < T_0$ is referred to as Phase I. The absence of anomalies at T_0 in the AC magnetic susceptibility and in NQR and NMR spectra suggests a nonmagnetic origin of the transition [5, 9], although recent experiments for a high-quality sample indicate the emergence of antifer-

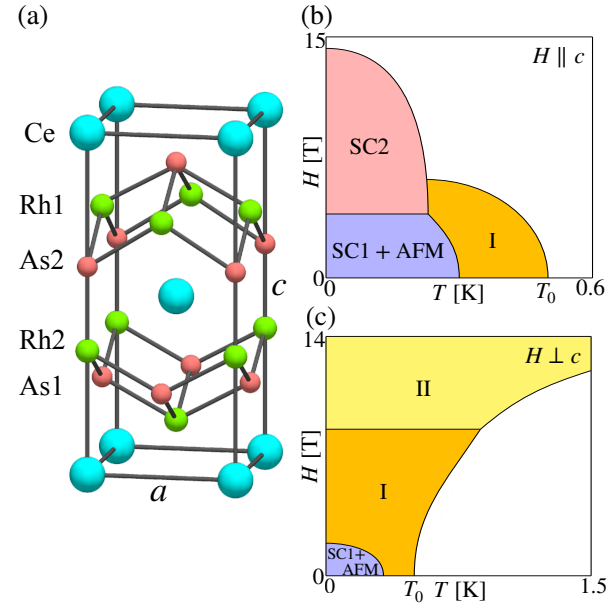


FIG. 1. (a) Crystal structure of CeRh₂As₂ and schematic T – H phase diagrams based on experimental results in magnetic field applied along (b) the c -axis [2] and (c) the in-plane direction [3].

romagnetic moments in Phase I [6, 42, 43]. A striking aspect of this transition is its strongly anisotropic response to the magnetic field: T_0 is strongly suppressed by $H \parallel c$ [1, 2, 43], while T_0 is enhanced by the in-plane magnetic field [3, 42] as shown in Figs. 1(b) and 1(c). The magnetic-field enhancement of the transition temperature is reminiscent of CeB₆, in which the antiferro-quadrupolar order is stabilized by the field-induced magnetic octupoles, although no such anisotropy is present there [44, 45]. Resistivity measurements in CeRh₂As₂ further suggest a transition into another phase, termed Phase II, under magnetic field $H \perp c$ [3]. Furthermore, a non-Fermi-liquid behavior has been observed in the paramagnetic state above $T = T_0$ [46, 47].

Two scenarios have been considered as the origin of Phase I. Hafner *et al.* proposed a quadrupole density wave (QDW) order that may emerge due to a nesting of the Fermi surfaces obtained from the renormalized band-structure calculations [3, 48]. The crystalline-electric-field (CEF) splitting divides the sextet of $j = 5/2$ into three doublets, with the ground-state and first-excited doublets separated by $\Delta_1 = 30$ K. Quadrupole degrees of freedom become active only when the first-excited doublet is involved, which can occur under sufficiently strong hybridization. Indeed, the Kondo temperature is estimated to be $T_K \approx 30$ K [1], comparable to Δ_1 . The X-ray absorption spectra indicate the formation of a quasi-quartet [49]. Symmetry analyses have also discussed possible quadrupolar order parameters [50].

On the other hand, Schmidt and Thalmeier discussed an antiferromagnetic order [51, 52]. In their scenario, the observed anisotropy with respect to the applied magnetic field is attributed to fluctuations of quadrupole moments induced by the magnetic field. By introducing interactions between xy -type quadrupoles, they demonstrated that the anisotropy of the experimental phase diagram can be reproduced within an antiferromagnetic ordering of in-plane moments. We note, however, that the antiferromagnetic and quadrupolar interactions are introduced *ad hoc*.

In this paper, we address the order parameter in Phase I of CeRh₂As₂, taking the electronic structure and strong correlations among 4f electrons into account. Our strategy consists of two steps. First, we derive the multipolar susceptibilities and effective interactions using density functional theory combined with dynamical mean-field theory (DFT+DMFT). A few candidate order parameters are listed at this stage. Next, we examine the anisotropy of the transition temperature. Combining a phenomenological argument with the DFT+DMFT results, we identify an order parameter that simultaneously exhibits strong fluctuations and reproduces the observed anisotropy. In this way, we propose a two-dimensional antiferromagnetic order of magnetic moments parallel to the c axis with $\mathbf{q} = (1/2, 1/2, 0)$ for the primary candidate, and an antiferromagnetic order of in-plane moments with $\mathbf{q} = (0, 0, 1/2)$ as a subleading candidate.

This paper is organized as follows. Section II presents a

construction of a low-energy model based on DFT calculations, and discusses the single-particle excitation spectrum by the DFT+DMFT method. In Sec. III, we derive the momentum-dependent multipolar susceptibilities and effective interactions. Taking the anisotropy of the transition temperature into account, we identify the order parameter in Sec. IV. Relations to experimental results and previous theoretical proposals are discussed in Sec. V. The paper is summarized in Sec. VI.

II. ELECTRONIC STRUCTURE

A. DFT calculations

We begin by calculating the electronic structure of CeRh₂As₂. The structure parameters are provided in Ref. [1]. We employ the full-potential local orbitals (FPLO) package [53, 54] with the generalized gradient approximation to calculate a fully relativistic band structure. The Brillouin zone is discretized into $48 \times 48 \times 24$ \mathbf{k} -points. 4f electrons of Ce ions are treated as itinerant. Figure 2 shows the DFT band structure (black lines) and density of states. This calculated electronic structure is in close agreement with the previous full-potential linearized augmented-plane-wave (FLAPW) results for CeRh₂As₂ [19]. To construct a low-energy model, we employ symmetry-protected maximally projected Wannier functions [55, 56], yielding a 124-band tight-binding model consisting of Ce 4f, 5d and 6s, Rh 4d and 5s, and As 4p orbitals. The resulting tight-binding bands [red lines in Fig. 2(a)] reproduce the DFT dispersion accurately.

We discuss the crystalline-electric field (CEF) states of 4f electrons. The $j = 5/2$ sextet splits into three Kramers doublets under the CEF with point-group symmetry C_{4v} . From the magnetic susceptibility and specific-heat measurements, the CEF level scheme shown in Fig. 3(a) has been proposed [3]. The ground state is the Γ_7 doublet, which is denoted by $\Gamma_7^{(1)}$. The first excited state is Γ_6 doublet, separated by $\Delta_1 = 30$ K. The second excited state is another Γ_7 , labeled $\Gamma_7^{(2)}$, lying $\Delta_2 = 180$ K above the ground state.

Our DFT results yield the CEF level scheme shown in Fig. 3(b). The two low-lying doublets are inverted compared to the experimental scheme. The energy splitting obtained is $\Delta_1 = -290$ K (the negative sign indicating the reversed order of $\Gamma_7^{(1)}$ and Γ_6). Since the CEF states play a dominant role in subsequent calculations of multipolar fluctuations, we artificially adjust the CEF potential to reproduce the experimental CEF level scheme.

B. DMFT calculations

We treat the strong correlations among 4f electrons in the DMFT [57, 58]. For simplicity, we omit the $j = 7/2$

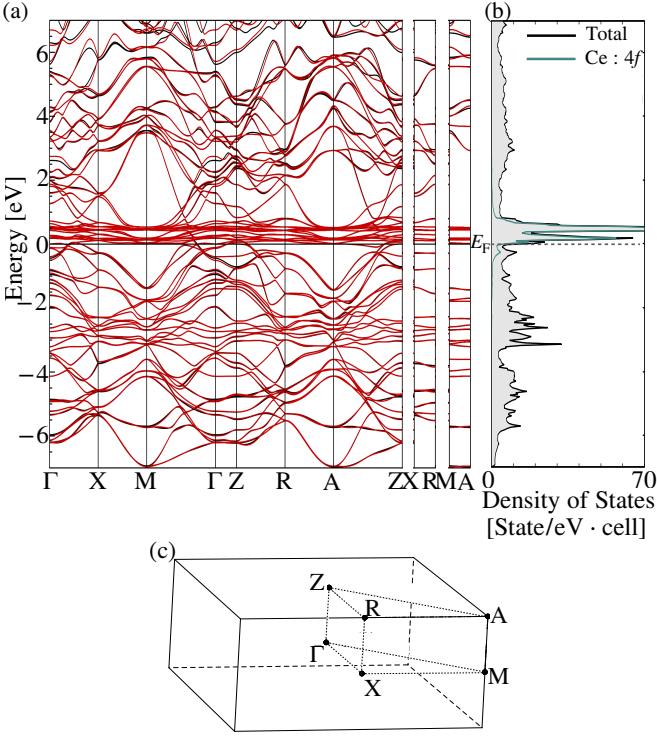


FIG. 2. (a) Fully relativistic band structure of CeRh_2As_2 calculated by FPLO package. The black lines represent the DFT result, and the red lines represent the tight-binding bands obtained from projective Wannier functions. (b) Density of states. The black and green lines show the total and Ce 4f contributions, respectively. (c) The high-symmetry points in the Brillouin zone.

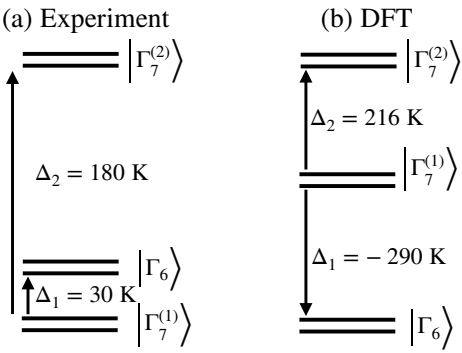


FIG. 3. The CEF level schemes of $j = 5/2$ of 4f electrons. (a) The experimental one [3], and (b) the DFT result. Δ_1 and Δ_2 denote the energy of Γ_6 and $\Gamma_7^{(2)}$ states, respectively, relative to $\Gamma_7^{(1)}$ state.

states of 4f electrons, which lie $\Delta_{\text{SOC}} \simeq 0.33$ eV above the $j = 5/2$ states due to the spin-orbit coupling. The single-particle Green's function for the remaining 108 or-

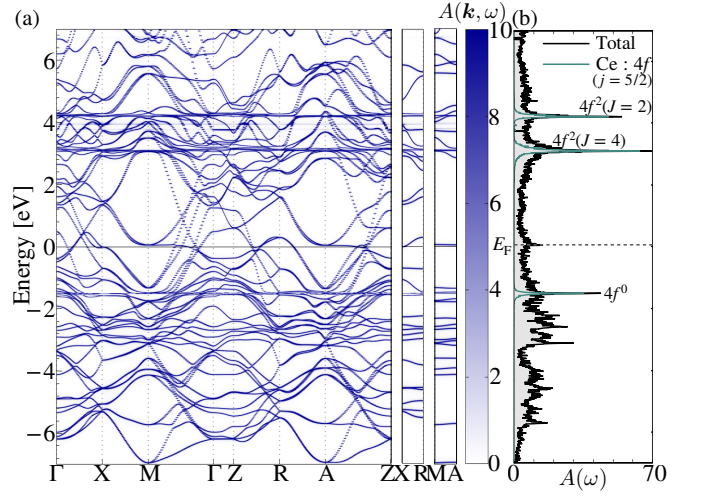


FIG. 4. (a) The single-particle excitation spectrum $A(\mathbf{k}, \omega)$ and (b) the \mathbf{k} -integrated spectrum $A(\omega)$ computed in DFT+DMFT method.

bitals is given by

$$\hat{G}(\mathbf{k}, i\omega_n) = \left[(i\omega_n + \mu) \hat{I} - \hat{H}_{\text{DFT}}(\mathbf{k}) - \hat{H}_{\text{CEF}} - \hat{\Sigma}_{\text{loc}}(i\omega_n) - \varepsilon_f \hat{P}_f \right]^{-1},$$

where the hat denotes a matrix having site, spin, and orbital indices within a unit cell. \hat{I} is the identity matrix. $\hat{H}_{\text{DFT}}(\mathbf{k})$ is the tight-binding Hamiltonian obtained by the DFT calculations, where the CEF potential for 4f electrons is removed. \hat{H}_{CEF} is the CEF potential that reproduces the experimental CEF level scheme in Fig. 3(a). We adopt this simple approach, although enforcing charge self-consistency between DFT and DMFT would improve the CEF potential [59, 60]. $\hat{\Sigma}_{\text{loc}}(i\omega_n)$ is the local self-energy in the DMFT. ε_f is the energy of the 4f levels. \hat{P}_f denotes a projection operator onto 4f orbitals. This term works as a double-counting correction between DFT and DMFT calculations.

We compute the self-energy $\hat{\Sigma}_{\text{loc}}$ using the exact diagonalization within the Hubbard-I approximation. Here, we adopt the fully rotationally invariant Coulomb interaction with the conventional parameterization [61]. The interaction parameters together with ε_f are chosen to reproduce the experimental spectrum as follows. The 4f level is set to $\varepsilon_f = -1.65$ eV to reproduce the ARPES experiments, which show the $4f^1 \rightarrow 4f^0$ excitation at $\Delta_- = 1.5$ eV below the Fermi level [14]. The direct Coulomb interaction is taken as $U = 5.8$ eV with the Hund's coupling $J = 0.8$ eV [62], to reproduce the $4f^1 \rightarrow 4f^2$ excitation energy $\Delta_+ = 3.1$ eV for elemental cerium [63].

Figure 4 shows the single-particle excitation spectrum thus obtained in DFT+DMFT calculations. The itinerant 4f band near E_F in the DFT [Fig. 2(a)] is now located around -1.5 eV and 3.1 eV, indicating a localized nature of 4f electrons. The resultant band structure near

E_F agrees with the DFT results for LaRh_2As_2 [64]. In particular, our results well reproduce the van Hove singularity near the Fermi level at the X point observed in the ARPES measurements [13].

III. MULTIPOLAR SUSCEPTIBILITIES AND INTERACTIONS

A. Method

We consider spin, charge, and orbital fluctuations within the DMFT. The momentum-dependent susceptibility is defined by

$$\chi_{im_1m_2,jm_3m_4}(\mathbf{q}) = \int_0^\beta d\tau \langle O_{im_1m_2}(\mathbf{q}, \tau) O_{jm_3m_4}(-\mathbf{q}) \rangle, \quad (1)$$

where $O_{im_1m_2}(\mathbf{q})$ is the Fourier transform of the local density operator

$$O_{im_1m_2}(\mathbf{R}) = f_{im_1}^\dagger(\mathbf{R}) f_{im_2}(\mathbf{R}). \quad (2)$$

Here, \mathbf{R} is the lattice vectors locating the origin of each unit cell, i labels the site in the unit cell, and m_1 denotes the z component of $j = 5/2$.

In DMFT, $\chi(\mathbf{q})$ can be computed by solving the Bethe-Salpeter equation for the two-particle Green's function [57]. In this paper, we employ an alternative approximate formula that avoids the explicit calculation of the two-particle vertex [65]. In this strong-coupling limit (SCL) formula, $\chi(\mathbf{q})$ is given by

$$\hat{\chi}(\mathbf{q}) = [\hat{\chi}_{\text{loc}}^{-1} - \hat{I}(\mathbf{q})]^{-1}, \quad (3)$$

where the hat denotes a matrix with respect to the combined indices im_1m_2 and jm_3m_4 . Here, $\hat{\chi}_{\text{loc}}$ is the local susceptibility evaluated from the effective impurity problem in DMFT, and $\hat{I}(\mathbf{q})$ describes the effective intersite interactions. The latter is computed from $\hat{G}(\mathbf{k}, i\omega_n)$ together with a function $\phi(i\omega_n)$, which effectively replaces the vertex function. We adopt the two-pole approximation for $\phi(i\omega_n)$ (referred to as the SCL3 scheme), in which $\phi(i\omega_n)$ is represented in terms of two poles located at Δ_- and Δ_+ , corresponding to the excitation energies from $4f^1$ configuration to $4f^0$ and $4f^2$, respectively [65]. This scheme successfully reproduces the antiferro-quadrupolar order in CeB_6 and the ferromagnetism in CeRh_6Ge_4 [66, 67]. A related approach based on the Hubbard-I approximation has also been developed [68, 69].

After all components of $\chi_{im_1m_2,jm_3m_4}(\mathbf{q})$ are obtained, we diagonalize it as follows:

$$\begin{aligned} \chi^{(\xi)}(\mathbf{q}) &= \sum_{ij} \sum_{m_1, \dots, m_4} \\ &\times u_{im_1m_2}^{(\xi)}(\mathbf{q}) \chi_{im_1m_2,jm_3m_4}(\mathbf{q}) u_{jm_3m_4}^{(\xi)}(\mathbf{q})^*. \end{aligned} \quad (4)$$

Here, eigenmodes are labeled with the superscript ξ . The eigenvalues $\chi^{(\xi)}(\mathbf{q})$ represent the magnitude of the fluctuations, and the eigenvectors $u_{im_1m_2}^{(\xi)}(\mathbf{q})$ represent the corresponding magnetic and orbital configuration.

The character of the fluctuations is identified as follows. We first construct the symmetry-adapted multipole basis (SAMB) $O^{(\gamma)}$ using open-source software `MultiPie` [70] as

$$O^{(\gamma)} = \sum_{imm'} z_{imm'}^{(\gamma)} O_{imm'}. \quad (5)$$

Each basis γ belongs to one of the irreducible representations in the crystallographic point group. We then project the eigenvector $u_{im_1m_2}^{(\xi)}(\mathbf{q})$ onto the SAMB by

$$c_\gamma^{(\xi)}(\mathbf{q}) = \sum_{im_1m_2} z_{im_1m_2}^{(\gamma)*} u_{im_1m_2}^{(\xi)}(\mathbf{q}). \quad (6)$$

At high-symmetry \mathbf{q} points defined in Fig. 2(c), the coefficients $c_\gamma^{(\xi)}(\mathbf{q})$ become finite exclusively in one irreducible representation. In contrast, at generic \mathbf{q} points, the coefficients belonging to different irreducible representations can take finite values. We therefore label each eigenmode ξ by the irreducible representation γ that has the largest weight $|c_\gamma^{(\xi)}(\mathbf{q})|^2$.

B. Multipoles

We perform a symmetry analysis of possible fluctuation modes using multipoles, which enables systematic characterization of symmetry-broken states [45] and the associated cross-correlated responses [71]. In the group theory, the operators within the Γ_7 doublet are decomposed as follows:

$$\Gamma_7 \otimes \Gamma_7 = A_1^+ \oplus A_2^- \oplus E^-, \quad (7)$$

where the superscript + (−) indicates the time-reversal even (odd) component, which appears by a symmetric (antisymmetric) product between two irreducible representations [72]. These operators are summarized in Table I (the second column). A_1^+ corresponds to the charge operator Q_0 , and A_2^- and E^- correspond to magnetic dipoles M_z and $\{M_x, M_y\}$, respectively.

We next consider multipoles that appear by mixing of the ground-state doublet $\Gamma_7^{(1)}$ and the first-excited doublet Γ_6 . The symmetries of the multipole operators are represented as

$$\Gamma_7 \otimes \Gamma_6 = B_1^\pm \oplus B_2^\pm \oplus E^\pm, \quad (8)$$

where the superscript \pm indicates that both charge and magnetic operators exist. The third column of Table I summarizes these operators. The charge operators in B_1^+ , B_2^+ , and E^+ are electric quadrupoles of $Q_{x^2-y^2}$, Q_{xy} , and $\{Q_{yz}, Q_{zx}\}$, respectively. The remaining quadrupole,

TABLE I. Atomic multipoles of $4f$ electrons. The column “irrep” indicates the irreducible representation of the C_{4v} point group. The second and third columns show the four multipoles in the Γ_7 doublet system and the additional twelve multipoles that appear in Γ_7 – Γ_6 pseudo-quartet system, respectively. The notation follows Ref. [71].

irrep	$\Gamma_7 \otimes \Gamma_7$	$\Gamma_7 \otimes \Gamma_6$
A_1^+	Q_0	$Q_{3z^2-r^2}$
A_2^+	–	–
B_1^+	–	$Q_{x^2-y^2}$
B_2^+	–	Q_{xy}
E^+	–	$\{Q_{yz}, Q_{zx}\}$
A_1^-	–	–
A_2^-	M_z	$M_{z(5z^2-3r^2)}$
B_1^-	–	M_{xyz}
B_2^-	–	$M_{z(x^2-y^2)}$
E^-	$\{M_x, M_y\}$	$\{M_{x(x^2-z^2)}, M_{y(y^2-z^2)}\},$ $\{M_{x(5x^2-3r^2)}, M_{y(5y^2-3r^2)}\}$

namely $Q_{3z^2-r^2}$, appears as a higher-order charge distribution in A_1^+ representation. The magnetic operators in B_1^- , B_2^- , and E^- correspond to magnetic octupoles. In addition, octupole operators also appear as higher-rank operators of M_x , M_y , and M_z .

Thus, within the $\Gamma_7^{(1)}$ doublet, there are four multipoles (charge and magnetic dipoles), while the $\Gamma_7^{(1)}$ – Γ_6 pseudo-quartet system additionally hosts five electric quadrupoles and seven magnetic octupoles. The two Ce sites in a unit cell allow either ferroic (F) or antiferroic (AF) configurations. Hereafter, we represent the combined atomic multipoles and the site degrees of freedom, for example, by M_z (F) and M_z (AF). For reference, we provide a symmetry classification based on cluster multipoles in Appendix A.

C. Results for susceptibilities

Figure 5 shows the eigenvalues $\chi^{(\xi)}(\mathbf{q})$ on the \mathbf{q} -path that connects the symmetry points in the Brillouin zone. There are 72 modes, which are composed of $6^2 = 36$ atomic degrees of freedom times two cerium atoms in a unit cell. The structure of this graph can be understood in terms of the CEF states. The six fluctuation modes in the top group are due to fluctuations within the ground-state doublet $\Gamma_7^{(1)}$, which has $2^2 - 1 = 3$ local degrees of freedom except for the charge fluctuation. The second group with 16+2 fluctuation modes arises from mixing between the ground-state and first-excited doublets. The third group is the fluctuations within the thermally excited Γ_6 state.

We focus on the first group in Fig. 5. Figure 6 shows $\chi^{(\xi)}(\mathbf{q})$ with symmetry characters distinguished by colors and symbols. The six fluctuation modes correspond to ferroic (F) or antiferroic (AF) configurations of the magnetic dipole (M_x , M_y , M_z) on the two cerium sites in a unit cell. The leading instabilities occur in M_z at

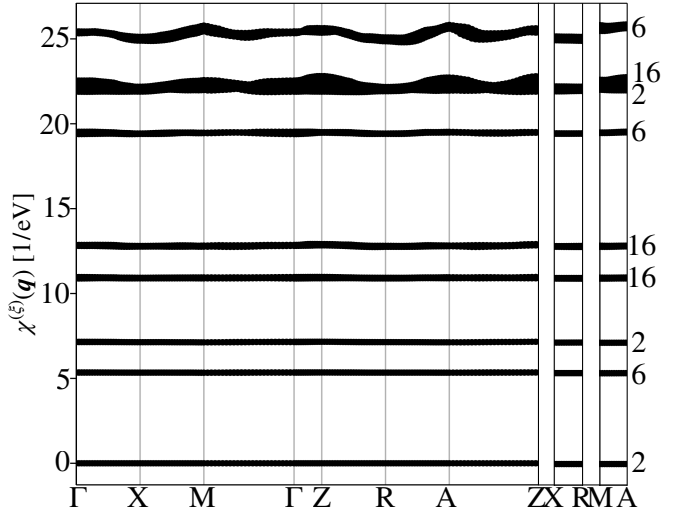


FIG. 5. Eigenvalues $\chi^{(\xi)}(\mathbf{q})$ of the susceptibility for $T = 0.01$ eV. The numbers on the right indicate the number of eigenmodes included in the group.

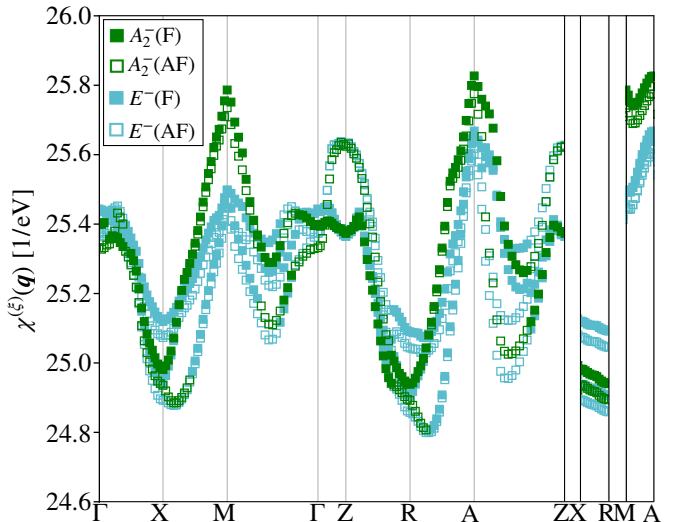


FIG. 6. Eigenvalues $\chi^{(\xi)}(\mathbf{q})$ of the susceptibility that correspond to fluctuations within $\Gamma_7^{(1)}$ doublet.

$\mathbf{q} = \mathbf{Q}_A \equiv (1/2, 1/2, 1/2)$ and $\mathbf{q} = \mathbf{Q}_M \equiv (1/2, 1/2, 0)$ with nearly equal intensity, indicating a weak interlayer coupling between Ce sites. Moreover, F and AF configurations are degenerate within numerical accuracy, suggesting that two Ce sites in a unit cell are effectively uncorrelated. These results indicate a two-dimensional checkerboard magnetic structure shown in Fig. 7, with only weak interlayer coupling along the c axis.

We next discuss the fluctuations in the second group that arise from the mixing of $\Gamma_7^{(1)}$ and Γ_6 . Figure 8 shows an enlarged plot of the eigenvalues $\chi^{(\xi)}(\mathbf{q})$ in the second group with additional symmetry labels. Electric and magnetic modes are plotted separately in Fig. 8(a) and Fig. 8(b), respectively. The largest fluctuation arises

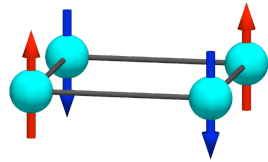


FIG. 7. Two-dimensional checkerboard type magnetic structure exhibiting the largest fluctuations in DFT+DMFT calculations.

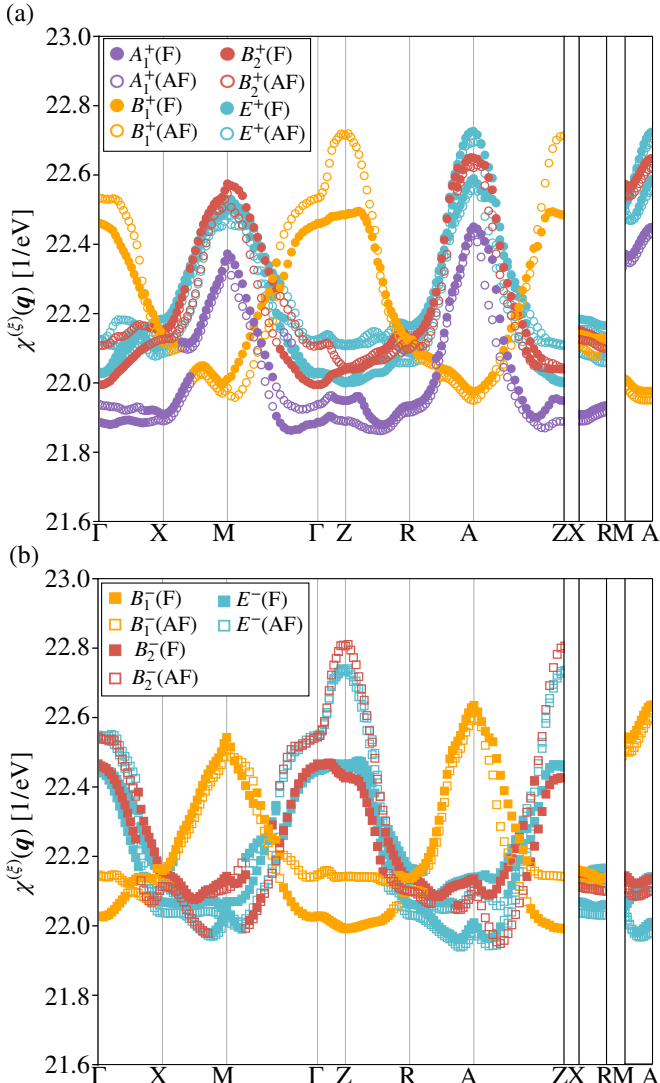


FIG. 8. Eigenvalues $\chi^{(\xi)}(\mathbf{q})$ of the susceptibility within the second group that corresponds to fluctuations between $\Gamma_7^{(1)}$ and Γ_6 states. (a) Electric modes and (b) magnetic modes.

in the magnetic modes [Fig. 8(b)] with the octupole $M_{z(x^2-y^2)}(\text{AF})$ in B_2^- symmetry at $\mathbf{q} = \mathbf{Q}_Z \equiv (0, 0, 1/2)$. Magnetic dipoles $\{M_x, M_y\}(\text{AF})$ follow this fluctuation. In the electric modes [Fig. 8(a)], the leading fluctuations are the quadrupoles $Q_{x^2-y^2}(\text{AF})$ in B_1^+ representation at $\mathbf{q} = \mathbf{Q}_Z$ and $\{Q_{yz}, Q_{zx}\}$ in E^+ representation at $\mathbf{q} = \mathbf{Q}_A$.

D. Results for multipolar interactions

We derive the effective interactions between multipoles. This quantity allows us to access lower temperatures (next subsection) and to discuss the magnetic-field dependence of the transition temperature (next section). The multipolar interactions are obtained by transforming $\hat{I}(\mathbf{q})$ into the SAMB representation. For a given basis γ , the effective interaction is computed as

$$I^{(\gamma)}(\mathbf{q}) = \sum_{ij} \sum_{m_1, \dots, m_4} z_{im_1 m_2}^{(\gamma)}(\mathbf{q}) I_{im_1 m_2, jm_3 m_4}(\mathbf{q}) z_{jm_3 m_4}^{(\gamma)}(\mathbf{q})^*. \quad (9)$$

Figure 9(a) shows interactions between the magnetic dipoles in the ground-state doublet $\Gamma_7^{(1)}$, whereas Figs. 9(b) and 9(c) show the interactions between the electric quadrupoles and magnetic octupoles, which arise from the mixing between the ground-state and first-excited doublets. The \mathbf{q} -dependence closely follows that in $\chi^{(\gamma)}(\mathbf{q})$. The magnitude of the interaction is of the order of 1 meV. We remark that the interactions involving quadrupoles and octupoles are stronger than those between dipoles. In particular, the electric quadrupole $Q_{x^2-y^2}(\text{AF})$ at $\mathbf{q} = \mathbf{Q}_Z$ and the magnetic octupole $M_{z(x^2-y^2)}(\text{AF})$ at $\mathbf{q} = \mathbf{Q}_Z$ exhibit especially strong interactions. This implies that fluctuations of the induced higher-order multipoles are expected to play some significant role.

E. Temperature dependence

So far, we presented results for a fixed temperature of $T = 0.01$ eV. We now discuss the temperature dependence of the susceptibilities and determine the transition temperature. As indicated in Eq. (3), $\hat{\chi}(\mathbf{q})$ consists of two contributions: the local susceptibility $\hat{\chi}_{\text{loc}}$ and the effective intersite interaction $\hat{I}(\mathbf{q})$. Previous work on CeB₆ has shown that the temperature dependence is dominated by $\hat{\chi}_{\text{loc}}$, allowing $\hat{I}(\mathbf{q})$ to be treated as effectively temperature independent [66].

Figure 10 shows the temperature dependence of the eigenvalues $\chi_{\text{loc}}^{(\xi)}$ of $\hat{\chi}_{\text{loc}}$. The leading eigenmodes are six-fold degenerate, corresponding to the magnetic dipoles within the CEF ground-state doublet at the two Ce sites in the unit cell. At high temperatures $T > \Delta_2$, the behavior follows the Curie-Weiss law

$$\chi_{\text{loc}}^{(\xi)} \approx \frac{C_{\text{high}}}{T - \Theta}, \quad (10)$$

with the Curie constant $C_{\text{high}} = 1/6$. In contrast, at low temperatures $T < \Delta_1$, the susceptibility follows the Curie law

$$\chi_{\text{loc}}^{(\xi)} \approx \frac{C_{\text{low}}}{T}, \quad (11)$$

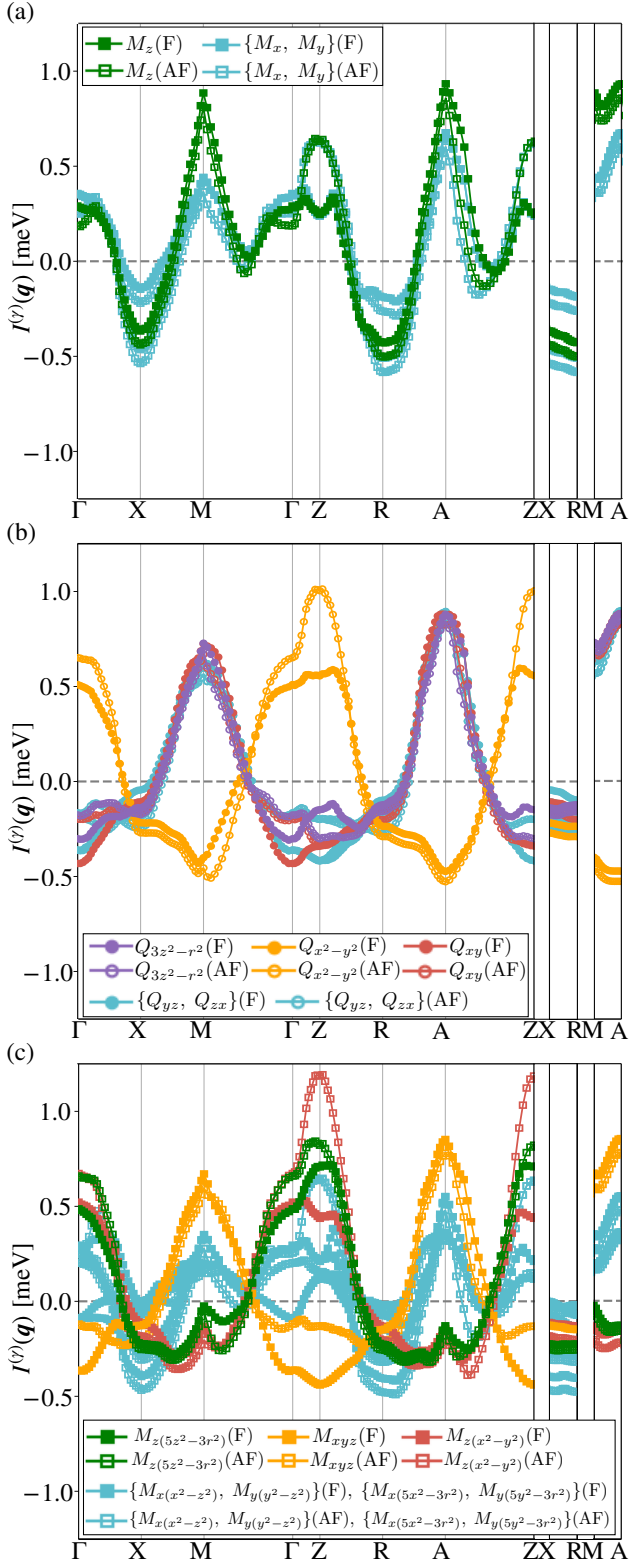


FIG. 9. The effective multipolar interactions $I^{(\gamma)}(\mathbf{q})$ for (a) magnetic dipoles, (b) electric quadrupoles, and (c) magnetic octupoles.

with $C_{\text{low}} = 1/2$. The lines in Fig. 10 indicate these

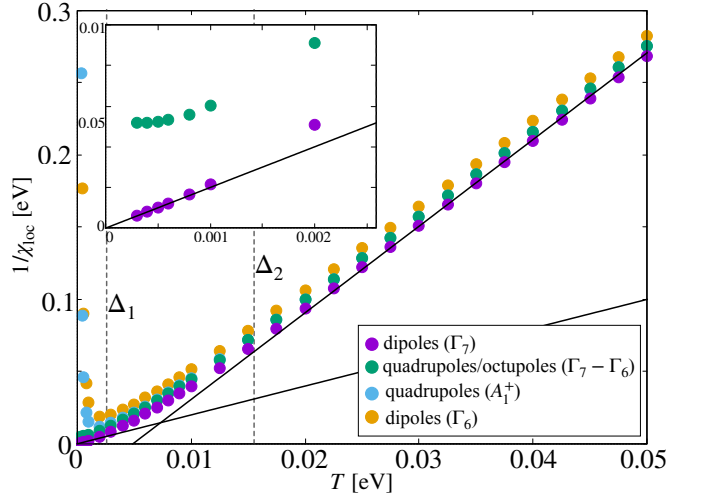


FIG. 10. Temperature dependence of the inverse of the eigenvalues of $\hat{\chi}_{\text{loc}}$. The solid lines show the Curie-Weiss law at high T and the Curie law at low T . The vertical dashed lines indicate the energy of the CEF excited states in Fig. 3(a).

asymptotic behaviors.

At high-symmetry \mathbf{q} points, the multipole basis γ can be chosen to coincide with the eigenmode ξ , since different irreducible representations do not mix. In this case, the matrix equation (3) decouples into an equation for each eigenmode ξ as

$$\chi^{(\xi)}(\mathbf{q}) = \frac{1}{(\chi_{\text{loc}}^{(\xi)})^{-1} - I^{(\gamma)}(\mathbf{q})}. \quad (12)$$

Using Eq. (11) and the value of $I^{(\gamma)}(\mathbf{q})$ evaluated at a given temperature, we can estimate the transition temperature from the divergence of $\chi^{(\xi)}(\mathbf{q})$. For the leading fluctuation mode, namely, the magnetic dipole M_z at $\mathbf{q} = \mathbf{Q}_A$, we obtain $I^{(\gamma)}(\mathbf{q}) = 0.93$ meV. The transition temperature is estimated to be 5.4 K, which is an order of magnitude larger than the experimental value $T_0 \approx 0.5$ K. Although DMFT commonly overestimates transition temperatures, the typical discrepancy is only a factor of 1.3–1.6 [66, 67]. The much larger deviation in the present case may indicate the influence of the Kondo effect in CeRh_2As_2 , as suggested in Refs. [1, 49].

In Fig. 10, the susceptibilities of quadrupoles and octupoles saturate to a constant value at low temperatures. This behavior arises because these multipoles are generated through hybridization between the CEF ground state and the first-excited doublet, and therefore follow the van Vleck mechanism. An exception is the $Q_{3z^2-r^2}$ quadrupole belonging to A_1^+ representation. Its fluctuation is rapidly suppressed as the temperature is lowered below $T = \Delta_1$, similar to the fluctuations within the CEF excited doublet Γ_6 .

IV. ANISOTROPY OF T - H PHASE DIAGRAM

The T - H phase diagram in CeRh_2As_2 is highly anisotropic as schematically shown in Figs. 1(b) and 1(c): Phase I is suppressed by the external magnetic field along the c axis, while it is enhanced by the field in the a - b plane. Schmidt and Thalmeier attributed this anisotropy to the role of field-induced quadrupole Q_{xy} under antiferromagnetic order of $\{M_x, M_y\}$ [51]. Their discussions are based on the assumption that M_x and Q_{xy} both have antiferroic intersite interactions of comparable magnitude. Using the effective interactions presented in the previous section, we examine possible order parameters that can account for the anisotropy of the phase diagram.

A. Phenomenology

The enhancement of the transition temperature in a magnetic field has been investigated in the context of the quadrupolar ordering in CeB_6 . Following Ref. [44], we present a phenomenological description of the field-dependence of the transition temperature. We show below that the transition temperature depends on fluctuations of the induced multipoles, even in the presence of the CEF splitting.

We consider the Landau free energy $\mathcal{F}(\phi_1, \phi_2, m)$ as a function of the primary order parameter ϕ_1 , the magnetic moment m coupled to the external magnetic field, and the field-induced multipole ϕ_2 . Near the critical temperature, $\mathcal{F}(\phi_1, \phi_2, m)$ can be expanded up to the fourth order as follows:

$$\begin{aligned} \mathcal{F}(\phi_1, \phi_2, m) = F_0 + \frac{1}{2}\chi_1^{-1}(T)\phi_1^2 + B\phi_1^4 + \frac{1}{2}\chi_2^{-1}(T)\phi_2^2 \\ - Hm + \frac{1}{2}\chi_m^{-1}(T)m^2 - gm\phi_1\phi_2, \end{aligned} \quad (13)$$

where F_0 denotes the contribution independent of ϕ_1 , ϕ_2 , and m . The second and third terms describe a symmetry breaking for ϕ_1 . The coefficient $\chi_1(T)$ is the susceptibility for ϕ_1 in the paramagnetic state with $H = 0$. This ensures the usual relation $\partial^2\mathcal{F}/\partial\phi_1^2|_{\phi_1=0} = \chi_1^{-1}(T)$ [73]. We neglected the fourth-order terms in ϕ_2 and m , since we consider only the symmetry breaking of ϕ_1 . The first term on the second line corresponds to the Zeeman energy, which induces a uniform magnetic moment m along the field direction. The last term describes the coupling among ϕ_1 , ϕ_2 , and m . The coupling is allowed when the product $m\phi_1\phi_2$ is invariant under the symmetry operation of the crystal. The explicit combinations for ϕ_1 , ϕ_2 , and m will be presented later.

Minimization of \mathcal{F} with respect to ϕ_1 , ϕ_2 , and m yields coupled equations that determine the thermodynamic values of ϕ_1 , ϕ_2 , and m . The transition temperature $T_1(H)$ is given by the temperature at which the symmetry-broken solution for ϕ_1 vanishes. In the lowest

order of g , this condition reads

$$\left[\chi_1^{-1}(T) - \frac{g^2 H^2}{\chi_2^{-1}(T)\chi_m^{-2}(T)} \right]_{T=T_1(H)} = 0. \quad (14)$$

An explicit form of $T_1(H)$ depends on the form of $\chi_1(T)$ and $\chi_2(T)$. We consider two cases below.

We first discuss the case of CeB_6 , following Ref. [44]. The primary order parameter ϕ_1 and the induced moment ϕ_2 correspond to the electric quadrupole and the magnetic octupole, respectively. Both multipoles are active in the CEF ground-state quartet. In this case, the corresponding susceptibilities follow the Curie-Weiss law represented by

$$\chi_1^{-1}(T) = \frac{T}{C} - I_1, \quad (15)$$

$$\chi_2^{-1}(T) = \frac{T}{C} - I_2. \quad (16)$$

Here, χ_1 and χ_2 differ in the intersite interactions I_1 and I_2 , whereas the Curie constant C is common to both. By definition, the primary order parameter has a larger interaction, $I_1 > I_2$. Substituting these expressions into Eq. (14) and solving the resulting quadratic equation for $T_1(H)$, we obtain, to the lowest-order in g ,

$$\frac{T_1(H)}{T_1(0)} \simeq 1 + \left[\frac{1}{1 - I_2/I_1} \right] g^2 C^2 \chi_m(T_1(0))^2 h^2, \quad (17)$$

where $T_1(0) = CI_1$. We introduced the dimensionless magnetic field $h = H/T_1(0)$. The coefficient of the h^2 term is always positive, meaning that the induced moment enhances the $T_1(H)$ under the magnetic field. The magnitude of the enhancement depends on the ratio I_2/I_1 . To highlight the influence of the induced multipole, we introduce an enhancement factor defined by

$$\alpha_1 = \frac{1}{1 - I_2/I_1}. \quad (18)$$

In CeB_6 , the antiferro-quadrupolar phase of Q_{xy} type (Phase II) is enhanced under the magnetic field through the induced octupole of M_{xyz} type [44]. This behavior is ascribed to the relation $I_2/I_1 \approx 1$, which has been proven analytically [74] and demonstrated numerically [66, 75].

In the case of CeRh_2As_2 , the situation differs due to the CEF splitting. Suppose that the primary order parameter ϕ_1 is the magnetic dipole within the CEF ground-state doublet, then $\chi_1(T)$ follows the Curie-Weiss law as in Eq. (15). In contrast, the induced quadrupole arises from mixing between the ground-state and excited doublets. As a result, $\chi_2(T)$ does not follow the Curie-Weiss law but instead saturates to a constant at low temperatures, as shown in Fig. 10. Replacing $\chi_2(T)$ with $\chi_2(0)$ in Eq. (14) and using Eq. (15), we obtain

$$\frac{T_1(H)}{T_1(0)} = 1 + I_1 \chi_2(0) g^2 C^2 \chi_m(T_1(0))^2 h^2. \quad (19)$$

The enhancement factor α_2 is therefore given by

$$\alpha_2 = I_1 \chi_2(0). \quad (20)$$

In the next subsection, we discuss the order parameter of Phase I in CeRh_2As_2 based on the value of α_2 .

B. Application of DFT+DMFT results

We now incorporate our DMFT results into the above phenomenological description to discuss the experimentally determined anisotropic T – H phase diagram. In this analysis, we assume that the primary order parameter ϕ_1 corresponds to the magnetic dipole within the CEF ground-state doublet, and then the induced moment ϕ_2 is the electric quadrupole. The combinations of ϕ_1 , ϕ_2 , and m that are allowed from the symmetry are summarized in Table II. Here, ϕ_1 and ϕ_2 share the same ordering vector \mathbf{q} , whereas m is uniform. Figure 11 illustrates the configurations of three candidates for the magnetic structure and the induced quadrupoles under magnetic fields $H \parallel c$ and $H \perp c$.

For the magnetic moment M_z along the c axis, a magnetic field $H \parallel c$ induces the quadrupole of $Q_{3z^2-r^2}$, whereas a field $H \parallel a$ induces Q_{zx} . This follows from the fact that the product $\phi_1 \phi_2 m$, corresponding to $M_z(\mathbf{q})Q_{3z^2-r^2}(-\mathbf{q})M_z(\mathbf{0})$ or $M_z(\mathbf{q})Q_{zx}(-\mathbf{q})M_x(\mathbf{0})$, is invariant under spatial inversion, translation, and time-reversal operations. For the in-plane magnetic moment M_y , the magnetic field $H \parallel c$ induces Q_{yz} , while the field $H \parallel a$ induces Q_{xy} . For the magnetic dipole oriented along the [110] direction, denoted by M_{x+y} , the induced quadrupole is rotated by 45°, and the in-plane field induces $Q_{x^2-y^2}$.

From the DMFT results in the previous section, we evaluated the magnetic transition temperatures T_1 , the ratio of the intersite interactions I_2/I_1 , and the enhancement factor α_2 defined in Eq. (20). The results are summarized in Table II. In this analysis, we selected specific \mathbf{q} points that yield relatively large transition temperatures. We note that $\alpha_2 = 0$ in the case with the induced quadrupole $Q_{3z^2-r^2}$, because its local fluctuation is suppressed at low temperatures, which can be confirmed in Fig. 10. For the other types of induced quadrupoles, α_2 is finite since $\chi_2(0)$ remains finite owing to the van Vleck contribution. For positive values of I_2/I_1 , the enhancement factor α_2 tends to become large, reflecting the growth of the fluctuation $\chi_2(0)$ of the induced quadrupole.

In the experiments, the transition temperature is suppressed for $H \parallel c$ and enhanced for $H \perp c$ as schematically shown in Fig. 1. This behavior can be explained by a small enhancement factor α_2 for $H \parallel c$ and a large α_2 for $H \perp c$. Two cases are consistent with the experimental anisotropy. The first case is a primary magnetic dipole M_z with $\mathbf{q} = \mathbf{Q}_A$ or \mathbf{Q}_M , which exhibits the largest fluctuations as shown in Fig. 6. Figures 11(a)–(c) show this magnetic structure and the correspond-

ing field-induced quadrupoles under $H \parallel c$ and $H \perp c$. For $H \parallel c$, no enhancement of the transition temperature is expected, because the fluctuations of the induced quadrupole $Q_{3z^2-r^2}$ belonging to A_1^+ representation are suppressed with decreasing temperature as demonstrated in Fig. 10. In contrast, for $H \perp c$, the transition temperature can increase due to the enhanced fluctuations of the induced quadrupole Q_{zx} , which are strengthened by the antiferroic interactions $I_2 > 0$.

The other case is the in-plane dipole ordering $M_{x+y}(\text{AF})$ with $\mathbf{q} = \mathbf{Q}_Z$, illustrated in Fig. 11(d). Under $H \parallel c$, the interaction between the induced quadrupole $Q_{(x+y)z}$ is ferroic, $I_2 < 0$, leading to a suppression of its fluctuations [Fig. 11(e)]. In contrast, for $H \perp c$, the induced quadrupole $Q_{x^2-y^2}$ exhibits large (even larger than that for M_{x+y}) antiferroic interactions $I_2 > 0$, which enhance its fluctuations [Fig. 11(f)]. The difference in the effective interaction of the induced quadrupoles, therefore, accounts for the anisotropy observed in the phase diagram. We note that the configuration $M_{x+y}(\text{AF})$ differs from $M_{x+y}(\text{F})$. They are shown in Fig. 12. These two magnetic structures are inequivalent, because no mirror symmetry in the a – b plane passes through the Ce site. We also remark that the case with M_x and M_y moments lead to an anisotropy inconsistent with experiments, since the effective interactions between the induced quadrupoles Q_{xy} are ferroic.

Finally, a comment on the checkerboard magnetic structure with an in-plane moment is in order. As an example, we consider the M_y order with $\mathbf{q} = \mathbf{Q}_A$, which is illustrated in Fig. 11(g). The checkerboard magnetic structure of M_y is proposed in Ref. [51]. The induced quadrupole is Q_{yz} for $H \parallel c$ and Q_{xy} for $H \perp c$, as shown in Figs. 11(h) and 11(i), respectively. Table II shows that both induced quadrupoles are subject to antiferroic interactions of the same magnitude. Therefore, the anisotropy of the experimentally observed T – H phase diagram is not expected in this case.

V. DISCUSSION

A. Magnetic ordering scenario for Phase I

Based on the susceptibilities in Sec. III and the expected anisotropy of the transition temperature in Sec. IV, we propose two candidates for the order parameter in Phase I: The primary candidate is the two-dimensional checkerboard configuration of M_z as illustrated in Fig. 7, and the subleading one is the in-plane dipole ordering as illustrated in Fig. 12. We now focus on the former. This configuration is consistent with the inelastic neutron scattering experiments, which report intensities at $\mathbf{q} = \mathbf{Q}_M$ [15]. This translation vector can be accounted for by nesting of the quasi-two-dimensional Fermi surface in DFT calculations with localized 4f electrons. Our results support antiferromagnetic ordering as proposed by μ SR [6].

TABLE II. Candidates of the magnetic dipole order parameter ϕ_1 in Phase I, and the corresponding field-induced electric quadrupole ϕ_2 . The column “F/AF” indicates ferroic and antiferroic configurations within a unit cell, where the dashes indicate that F and AF are degenerate. The enhancement factor α_2 is defined in Eq. (20). $M_{x+y} = M_x + M_y$ and $Q_{(x+y)z} = Q_{yz} + Q_{zx}$ represent linear combinations of the multipoles belonging to E representation.

ϕ_1	F/AF	\mathbf{q}	T_1 [K]	direction of m	ϕ_2	I_2/I_1	α_2	direction of m	ϕ_2	I_2/I_1	α_2
M_z	—	\mathbf{Q}_A	5.4	[001]	$Q_{3z^2-r^2}$	0.94	0	[100]	Q_{zx}	0.96	0.22
	—	\mathbf{Q}_M	5.1			0.82	0			0.71	0.20
	AF	\mathbf{Q}_Z	3.7			-0.48	0			-0.32	0.12
M_y	—	\mathbf{Q}_A	3.9	[001]	Q_{yz}	1.3	0.16	[100]	Q_{xy}	1.3	0.16
	AF	\mathbf{Q}_Z	3.6			-0.32	0.12			-0.53	0.11
M_{x+y}	—	\mathbf{Q}_A	3.9	[001]	$Q_{(x+y)z}$	1.5	0.17	[110]	$Q_{x^2-y^2}$	-0.70	0.12
	AF	\mathbf{Q}_Z	3.6			-0.31	0.12			1.6	0.15

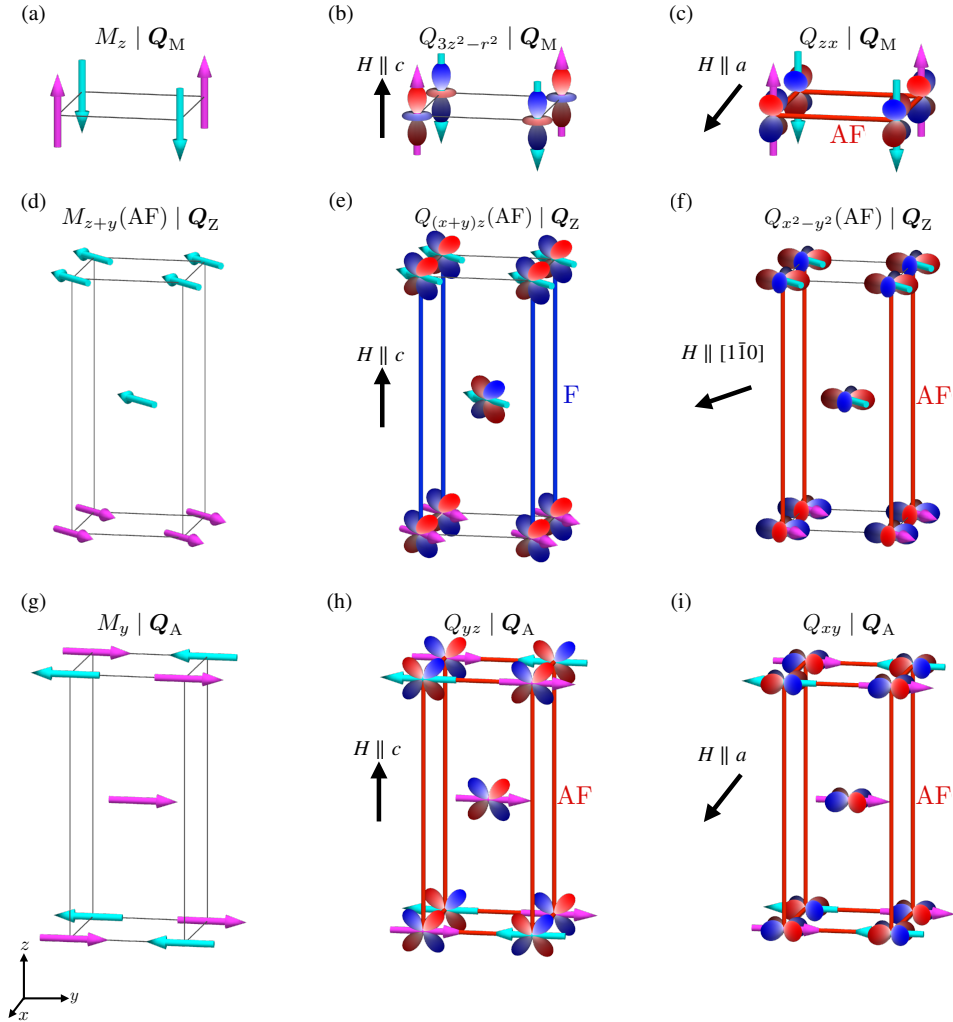


FIG. 11. Candidate magnetic structures and the induced quadrupoles under magnetic fields $H \parallel c$ and $H \perp c$. (a)–(c) M_z order with $\mathbf{q} = \mathbf{Q}_M$, (d)–(f) $M_{x+y}(\text{AF})$ order with $\mathbf{q} = \mathbf{Q}_Z$, and (g)–(i) M_y order with $\mathbf{q} = \mathbf{Q}_A$. The red and blue bonds represent the antiferroic and ferroic quadrupolar correlations, respectively. The labels such as $M_z | \mathbf{Q}_M$ indicate the ordered state of M_z at $\mathbf{q} = \mathbf{Q}_M$.

Upon the onset of this magnetic structure, the four-fold rotational symmetry is broken. As a consequence, the maximal magnetic space group in the ordered phase becomes $C_Pm'ma$ (No. 67.13.589 in OG) [76, 77]. In particular, the related magnetic point group is $mmm1'$,

i.e., a gray magnetic point group that still contains time-reversal symmetry. Importantly, this implies that all spatially averaged ($\mathbf{q} = \mathbf{0}$) time-reversal-odd quantities vanish, even though finite- \mathbf{q} magnetic order is present.

There are two degenerate configurations, $M_z(\text{F})$ and

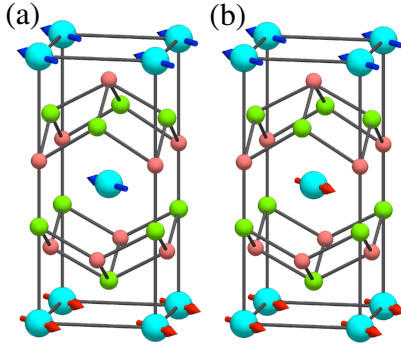


FIG. 12. The magnetic structure for (a) $M_{x+y}(\text{AF})$ and $M_{x+y}(\text{F})$ with $\mathbf{q} = \mathbf{Q}_Z$.

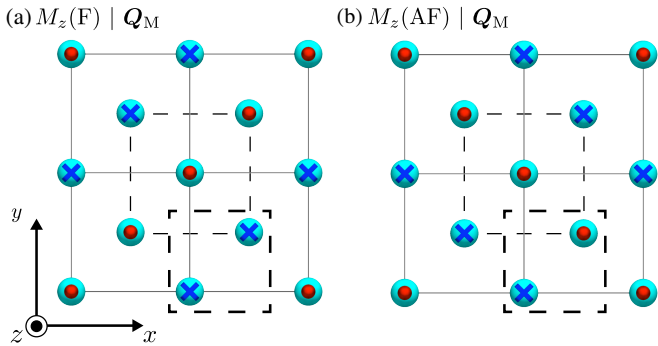


FIG. 13. Checkerboard-type magnetic structures at $\mathbf{q} = \mathbf{Q}_M$, as viewed from the z direction, with (a) ferroic and (b) antiferroic configurations in the unit cell (indicated by the enclosed thick dashed lines). The red dots and blue crosses indicate $+M_z$ and $-M_z$, respectively. Sites connected by thin solid (dashed) lines lie in the $z = 0$ ($z = 1/2$) plane. The labels follow the notation in Fig. 11.

$M_z(\text{AF})$, as illustrated in Fig. 13. From a symmetry point of view, the reduction of the magnetic point group from $4/mmm1'$ to $mmm1'$ allows an additional electric quadrupole component in the magnetically ordered phase [78]. Since the present magnetic structure has mirror symmetries perpendicular to the $[110]$ or $[\bar{1}\bar{1}0]$ directions, the xy -type electric quadrupole Q_{xy} (in the original crystal coordinate system) is permitted. Here, we introduce a domain parameter η as the intensity difference: $\eta \equiv |M_z(\text{F})|^2 - |M_z(\text{AF})|^2$. This domain parameter transforms as Q_{xy} and therefore couples linearly to the shear strain ε_{xy} . Consequently, a symmetry-allowed coupling term of the form $\lambda\varepsilon_{xy}\eta$ appears in the Landau free energy, implying that uniaxial strain applied along the $[110]$ direction lifts the degeneracy between the two domains. Therefore, when the system is cooled through T_0 under such strain, domain selection occurs in the ordered state, enabling statistical control of the checkerboard domains.

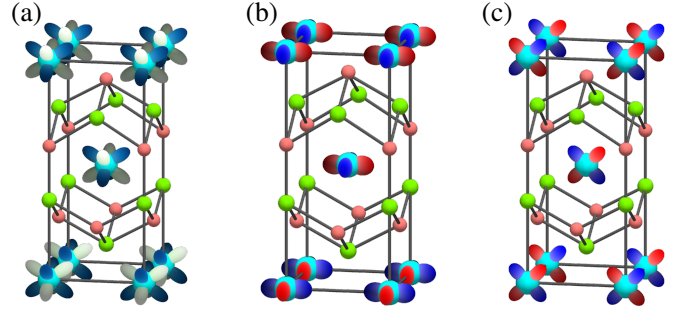


FIG. 14. Configurations corresponding to large fluctuations arising by hybridization between $\Gamma_7^{(1)}$ and Γ_6 . (a) The magnetic octupole $M_{z(x^2-y^2)}(\text{AF})$ at $\mathbf{q} = \mathbf{Q}_Z$, (b) electric quadrupole $Q_{x^2-y^2}(\text{AF})$ at $\mathbf{q} = \mathbf{Q}_Z$, and (c) electric quadrupole $\{Q_{yz}, Q_{zx}\}$ at $\mathbf{q} = \mathbf{Q}_A$. The different colors stand for the sign of the magnetic density in (a) and the sign of the charge density in (b) and (c).

B. Quadrupolar ordering scenario for Phase I

We consider here a quadrupolar ordering scenario that becomes feasible when the CEF excited doublet participates in the low-energy physics, for instance, by the Kondo effect. Once a pseudo-quartet is formed, the susceptibilities arising from hybridization between the CEF ground state $\Gamma_7^{(1)}$ and the excited state Γ_6 acquire significance. We therefore examine the quadrupole scenario based on the DFT+DMFT results shown in Fig. 8.

Hafner *et al.* proposed a quadrupolar density wave (QDW) of $Q_{3z^2-r^2}$ with an incommensurate translation vector $\mathbf{q} = (q_x, 0, 0)$ [3]. This state corresponds to the A_1^+ representation in our notation. In Fig. 8(a), however, the A_1^+ fluctuation is not enhanced along the Γ -X line relative to other quadrupole modes. Furthermore, the local fluctuations of the A_1^+ quadrupole rapidly vanish for $T < \Delta_1$, indicating that the incommensurate QDW is not favored within our localized $4f$ model. On the other hand, Harima proposed antiferro-quadrupolar order of Q_{xy} [50], which corresponds to $B_2^+(\text{AF})$ at $\mathbf{q} = \mathbf{Q}_\Gamma \equiv (0, 0, 0)$. In Fig. 8(a), this quadrupole mode exhibits pronounced fluctuations not at $\mathbf{q} = \mathbf{Q}_\Gamma$ but rather at $\mathbf{q} = \mathbf{Q}_A$. In our results, fluctuations at $\mathbf{q} = \mathbf{Q}_\Gamma$ remain generally weak, implying antiferroic correlations between Ce sites along the c axis.

From the DFT+DMFT results in Fig. 8, the leading instability in the pseudo-quartet system is the magnetic octupole $M_{z(x^2-y^2)}(\text{AF})$ at $\mathbf{q} = \mathbf{Q}_Z$, followed by the electric quadrupoles $Q_{x^2-y^2}(\text{AF})$ at $\mathbf{q} = \mathbf{Q}_Z$ and $\{Q_{yz}, Q_{zx}\}$ at $\mathbf{q} = \mathbf{Q}_A$. Figure 14 illustrates the magnetic and electric configurations corresponding to these fluctuations. Applying the method described in Sec. IV, we investigated how the magnetic field affects the transition temperature. We found, however, that none of these candidates yields the anisotropy consistent with the experiments. Further details are presented in Appendix B.

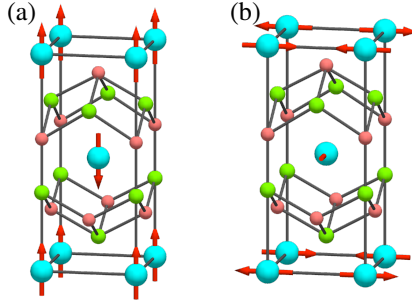


FIG. 15. Magnetic structures in AFM+SC1 phase proposed from NQR experiments [5]. (a) An AFM structure at $\mathbf{q} = \mathbf{Q}_\Gamma$, and (b) a helical structure at $\mathbf{q} = \mathbf{Q}_A$. The arrows indicate the magnetic dipole.

C. Magnetic structure in AFM+SC1 phase

Finally, we comment on two magnetic configurations in AFM+SC1 phase proposed from NQR experiments [5], assuming that the susceptibilities computed in the normal state remain applicable to the superconducting phase. One is the staggered AFM configuration depicted in Fig. 15(a), which corresponds in our notation to $M_z(\text{AF})$ with the translation vector $\mathbf{q} = \mathbf{Q}_\Gamma$. In our results (Fig. 6), however, the fluctuations at $\mathbf{q} = \mathbf{Q}_\Gamma$ exhibit no pronounced enhancement, which does not support the AFM configuration in Fig. 15(a). The other configuration proposed in the NQR study [5] is a helical structure of in-plane magnetic moments, illustrated in Fig. 15(b). This structure can be expressed as a linear combination of $E^-(\text{F})$ and $E^-(\text{AF})$, namely, $M_x(\text{AF}) - M_x(\text{F}) - M_y(\text{F}) - M_y(\text{AF})$ with $\mathbf{q} = \mathbf{Q}_A$. In Fig. 6, the corresponding fluctuations appear as the second leading instability. Thus, within our DFT+DMFT calculations, the helical magnetic structure shown in Fig. 15(b) appears as a subleading candidate.

VI. SUMMARY

We derived the momentum-dependent multipolar susceptibilities using the DFT+DMFT method, assuming localized $4f$ electrons. The energy of the $4f$ level and the interaction parameters were determined from photoemission spectra. The susceptibilities comprise 72 eigenmodes, classified into 36 atomic multipoles, each associated with ferroic or antiferroic configurations of two Ce sites in the unit cell. The symmetry of these eigenmodes was identified using a complete set of symmetry-adapted multipole bases.

Among all the fluctuation modes, the susceptibility corresponding to the two-dimensional checkerboard configuration of the M_z magnetic moment is the largest. This mode is consistent with the inelastic neutron scattering experiments [15]. Once higher-order multipoles arising from the hybridization between the CEF ground-

state and first-excited doublets are included, additional candidates appear as possible order parameters in Phase I if one relies solely on the susceptibility amplitudes. However, most of these candidates can be ruled out by requiring consistency with the characteristic anisotropy of the experimental T - H phase diagram. We thus concluded that the M_z dipole with $\mathbf{q} = \mathbf{Q}_M \equiv (1/2, 1/2, 0)$ is the most plausible, as it exhibits both the largest susceptibility and the correct anisotropic response to the magnetic field. The increase of T_0 under $H \perp c$ is attributed to the enhanced fluctuations of the field-induced quadrupole $\{Q_{yz}, Q_{zx}\}$, whereas no enhancement is expected for $H \parallel c$ because the field-induced quadrupole $Q_{3z^2-r^2}$ is not locally active. A subleading candidate is the antiferromagnetic order of the in-plane moment M_{x+y} with $\mathbf{q} = \mathbf{Q}_Z \equiv (0, 0, 1/2)$. Orderings of higher-order multipoles, including electric quadrupoles, do not reproduce the observed magnetic-field anisotropy in our DFT+DMFT results.

These results demonstrate an effective use of first-principles approaches in identifying the order parameter of multipolar order in realistic materials.

ACKNOWLEDGMENTS

We thank H. Kusunose for support regarding the MultiPie library. This work was supported by JSPS KAKENHI Grants No. 23H04869 and No. 25K22013. Part of the computations in this work were performed using the facilities of the Supercomputer Center, the Institute for Solid State Physics, the University of Tokyo (2024-Bb-0043, 2025-Ca-0086).

Appendix A: Symmetry classification of cluster multipoles

In the main text, the ferroic and antiferroic configurations within a unit cell are denoted by F and AF, respectively. When two multipoles are aligned in an AF manner, the symmetry of the resultant cluster multipole is different from the symmetry of the atomic multipole. Here, a cluster multipole refers to the combined object composed of multipoles within the unit cell. Classifying the symmetry of such cluster multipoles allows us to predict responses of the ordered state to external fields [71].

Table III shows the symmetry classification of the cluster multipoles derived using MultiPie [70]. The atomic multipoles correspond to those listed in Table I. For F configuration, the symmetry of the cluster multipoles is the same as the atomic multipole, apart from the additional subscript g indicating invariance under spatial inversion. For AF configuration, the spatial inversion is odd, indicated by the subscript u .

TABLE III. Cluster multipoles and their symmetry in CeRh_2As_2 . The “atomic” column lists the atomic multipoles, and “irrep(a)” gives the irreducible representation based on the site symmetry. The “F/AF” column denotes ferroic (F) and antiferroic (AF) configuration within the unit cell. The last two columns show the symbol of the cluster multipoles and the irreducible representation in the point group D_{4h} .

irrep(a)	atomic	F/AF	cluster	irrep(c)
A_1^+	$Q_0, Q_{3z^2-r^2}$	F	$Q_0, Q_{3z^2-r^2}$	A_{1g}^+
		AF	Q_z	A_{2u}^+
B_1^+	$Q_{x^2-y^2}$	F	$Q_{x^2-y^2}$	B_{1g}^+
		AF	G_{xy}	B_{2u}^+
B_2^+	Q_{xy}	F	Q_{xy}	B_{2g}^+
		AF	$G_{x^2-y^2}$	B_{1u}^+
E^+	$\{Q_{yz}, Q_{zx}\}$	F	$\{Q_{yz}, Q_{zx}\}$	E_g^+
		AF	$\{Q_x, Q_y\}$	E_u^+
A_2^-	$M_z, M_{z(5z^2-3r^2)}$	F	$M_z, M_{z(5z^2-3r^2)}$	A_{2g}^-
		AF	$M_0, M_{3z^2-r^2}$	A_{1u}^-
B_1^-	M_{xyz}	F	M_{xyz}	B_{1g}^-
		AF	M_{xy}	B_{2u}^-
B_2^-	$M_{z(x^2-y^2)}$	F	$M_{z(x^2-y^2)}$	B_{2g}^-
		AF	$M_{x^2-y^2}$	B_{1u}^-
E^-	$\{M_x, M_y\},$ $\{M_{x(x^2-z^2)}, M_{y(y^2-z^2)}\},$ $\{M_{x(5x^2-3r^2)}, M_{y(5y^2-3r^2)}\}$	F	$\{M_x, M_y\},$ $\{M_{x(x^2-z^2)}, M_{y(y^2-z^2)}\},$ $\{M_{x(5x^2-3r^2)}, M_{y(5y^2-3r^2)}\}$	E_g^-
		AF	$\{T_x, T_y\}$ $\{M_{yz}, M_{zx}\}$ $\{T_{x(5x^2-3r^2)}, T_{y(5y^2-3r^2)}\}$	E_u^-

TABLE IV. Candidates of the quadrupole or octupole order parameter ϕ_1 in Phase I, and the field-induced multipoles ϕ_2 . The enhancement factor α_1 is defined in Eq. (18). The dash in the column for α_1 means that Eq. (18) is not applicable because of $I_2(\mathbf{q})/I_1(\mathbf{q}) > 1$. See also the caption of Table II.

ϕ_1	F/AF	\mathbf{q}	field direction	ϕ_2	I_2/I_1	α_1	field direction	ϕ_2	I_2/I_1	α_1
$M_{z(x^2-y^2)}$	AF	\mathbf{Q}_Z	[001]	$Q_{x^2-y^2}$	0.85	6.5	[100]	Q_{zx}	-0.17	0.86
$Q_{x^2-y^2}$	AF	\mathbf{Q}_Z	[001]	$M_{z(x^2-y^2)}$	1.2	-	[100]	$M_{x(y^2-z^2)}$	0.15	1.2
								$M_{x(5x^2-3r^2)}$	0.63	2.7
Q_{zx}	-	\mathbf{Q}_A	[001]	$M_{x(y^2-z^2)}$	0.40	1.7	[100]	$M_{z(x^2-y^2)}$	-0.16	0.86
				$M_{x(5x^2-3r^2)}$	0.62	2.6		$M_{z(5z^2-3r^2)}$	-0.14	0.87

Appendix B: Anisotropy of quadrupolar ordering in pseudo-quartet model

Section IV discusses the anisotropy of the magnetic-field enhancement of the transition temperatures for the magnetic dipole order. Here, we apply the same analysis to the electric quadrupoles and magnetic octupoles, which arise from hybridization between the CEF ground-state and first-excited doublets.

Table IV shows the quadrupole and octupole counterparts of Table II. The three multipoles exhibiting the largest fluctuations in Fig. 8 are included. When ϕ_1 corresponds to the electric quadrupole, the induced moment

ϕ_2 is the magnetic octupole, and vice versa. The ratio I_2/I_1 is obtained from the results shown in Fig. 9. The enhancement factor α_1 is evaluated using Eq. (18), with the assumption that the two CEF doublets are degenerate and give rise to the Curie-Weiss behavior of the susceptibilities. We find, for all three cases, that the ratio I_2/I_1 is smaller for $H \perp c$ than for $H \parallel c$, resulting in a smaller enhancement factor for $H \perp c$. This tendency is opposite to the experiments, where the transition temperature T_0 is enhanced (suppressed) for $H \parallel c$ ($H \perp c$). Therefore, the DFT+DMFT results do not support the electric-quadrupole and magnetic-octupole scenario in the pseudo-quartet CEF system for Phase I.

[1] S. Khim, J. F. Landaeta, J. Banda, N. Bannor, M. Brando, P. M. R. Brydon, D. Hafner, R. Küchler, R. Cardoso-Gil, U. Stockert, A. P. Mackenzie, D. F. Agterberg, C. Geibel, and E. Hassinger, Field-induced transition within the superconducting state of CeRh_2As_2 ,

Science **373**, 1012 (2021).
[2] K. Semeniuk, D. Hafner, P. Khanenko, T. Lühmann, J. Banda, J. F. Landaeta, C. Geibel, S. Khim, E. Hassinger, and M. Brando, Decoupling multiphase superconductivity from normal state ordering in CeRh_2As_2 , Phys.

Rev. B **107**, L220504 (2023).

[3] D. Hafner, P. Khanenko, E.-O. Eljaouhari, R. Küchler, J. Banda, N. Bannor, T. Lüthmann, J. F. Landaeta, S. Mishra, I. Sheikin, E. Hassinger, S. Khim, C. Geibel, G. Zwicknagl, and M. Brando, Possible quadrupole density wave in the superconducting Kondo lattice CeRh₂As₂, *Phys. Rev. X* **12**, 011023 (2022).

[4] J. F. Landaeta, P. Khanenko, D. C. Cavanagh, C. Geibel, S. Khim, S. Mishra, I. Sheikin, P. M. R. Brydon, D. F. Agterberg, M. Brando, and E. Hassinger, Field-angle dependence reveals odd-parity superconductivity in CeRh₂As₂, *Phys. Rev. X* **12**, 031001 (2022).

[5] M. Kibune, S. Kitagawa, K. Kinjo, S. Ogata, M. Manago, T. Taniguchi, K. Ishida, M. Brando, E. Hassinger, H. Rosner, C. Geibel, and S. Khim, Observation of an antiferromagnetic order as odd-parity multipoles inside the superconducting phase in CeRh₂As₂, *Phys. Rev. Lett.* **128**, 057002 (2022).

[6] S. Khim, O. Stockert, M. Brando, C. Geibel, C. Baines, T. J. Hicken, H. Luetkens, D. Das, T. Shiroka, Z. Guguchia, and R. Scheuermann, Coexistence of local magnetism and superconductivity in the heavy-fermion compound CeRh₂As₂ revealed by μ SR studies, *Phys. Rev. B* **111**, 115134 (2025).

[7] S. Kitagawa, M. Kibune, K. Kinjo, M. Manago, T. Taniguchi, K. Ishida, M. Brando, E. Hassinger, C. Geibel, and S. Khim, Two-dimensional XY-type magnetic properties of locally noncentrosymmetric superconductor CeRh₂As₂, *J. Phys. Soc. Jpn.* **91**, 043702 (2022).

[8] S. Ogata, S. Kitagawa, K. Kinjo, K. Ishida, M. Brando, E. Hassinger, C. Geibel, and S. Khim, Parity transition of spin-singlet superconductivity using sublattice degrees of freedom, *Phys. Rev. Lett.* **130**, 166001 (2023).

[9] S. Ogata, S. Kitagawa, K. Kinjo, K. Ishida, M. Brando, E. Hassinger, C. Geibel, and S. Khim, Appearance of *c*-axis magnetic moment in odd-parity antiferromagnetic state in CeRh₂As₂ revealed by ⁷⁵As-NMR, *Phys. Rev. B* **110**, 214509 (2024).

[10] S. Ogata, S. Kitagawa, K. Ishida, M. Brando, E. Hassinger, C. Geibel, and S. Khim, Conventional *s*-wave superconductivity in LaRh₂As₂; the analog without the 4f electrons of CeRh₂As₂, *J. Phys. Soc. Jpn.* **95**, 013701 (2026).

[11] S.-i. Kimura, J. Sichelschmidt, and S. Khim, Optical study of the electronic structure of locally noncentrosymmetric CeRh₂As₂, *Phys. Rev. B* **104**, 245116 (2021).

[12] S. Onishi, U. Stockert, S. Khim, J. Banda, M. Brando, and E. Hassinger, Low-temperature thermal conductivity of the two-phase superconductor CeRh₂As₂, *Front. Electron. Mater.* **2**, 880579 (2022).

[13] X. Chen, L. Wang, J. Ishizuka, R. Zhang, K. Nogaki, Y. Cheng, F. Yang, Z. Chen, F. Zhu, Z. Liu, J. Mei, Y. Yanase, B. Lv, and Y. Huang, Coexistence of near- E_F flat band and Van Hove singularity in a two-phase superconductor, *Phys. Rev. X* **14**, 021048 (2024).

[14] B. Chen, H. Liu, Q.-Y. Wu, C. Zhang, X.-Q. Ye, Y.-Z. Zhao, J.-J. Song, X.-Y. Tian, B.-L. Tan, Z.-T. Liu, M. Ye, Z.-H. Chen, Y.-B. Huang, D.-W. Shen, Y.-H. Yuan, J. He, Y.-X. Duan, and J.-Q. Meng, Exploring possible Fermi surface nesting and the nature of heavy quasiparticles in the spin-triplet superconductor candidate CeRh₂As₂, *Phys. Rev. B* **110**, L041120 (2024).

[15] T. Chen, H. Siddiquee, Q. Xu, Z. Rehfuss, S. Gao, C. Lygouras, J. Drouin, V. Morano, K. E. Avers, C. J. Schmitt, A. Podlesnyak, J. Paglione, S. Ran, Y. Song, and C. Broholm, Quasi-two-dimensional antiferromagnetic spin fluctuations in the spin-triplet superconductor candidate CeRh₂As₂, *Phys. Rev. Lett.* **133**, 266505 (2024).

[16] H. Siddiquee, Z. Rehfuss, C. Broyles, and S. Ran, Pressure dependence of superconductivity in CeRh₂As₂, *Phys. Rev. B* **108**, L020504 (2023).

[17] K. Semeniuk, M. Pfeiffer, J. F. Landaeta, M. Nicklas, C. Geibel, M. Brando, S. Khim, and E. Hassinger, Exposing the odd-parity superconductivity in CeRh₂As₂ with hydrostatic pressure, *Phys. Rev. B* **110**, L100504 (2024).

[18] Q. Dong, T. Shi, P. Yang, X. Liu, X. Shi, L. Wang, J. Xiang, H. Ma, Z. Tian, J. Sun, Y. Uwatoko, G. Chen, X. Wang, J. Shen, R. Wu, X. Lu, P. Sun, G. Chajewski, D. Kaczorowski, B. Wang, and J. Cheng, Strong superconducting pairing strength and pseudogap features in a putative multiphase heavy-fermion superconductor CeRh₂As₂ studied by soft point contact spectroscopy, *Phys. Rev. B* **111**, L180501 (2025).

[19] K. Nogaki, A. Daido, J. Ishizuka, and Y. Yanase, Topological crystalline superconductivity in locally noncentrosymmetric CeRh₂As₂, *Phys. Rev. Res.* **3**, L032071 (2021).

[20] M. L. Ali, M. K. Alam, M. Khan, M. N. M. Nobin, N. Islam, U. Faruk, and M. Z. Rahaman, Pressure-dependent structural, electronic, optical, and mechanical properties of superconductor CeRh₂As₂: A first-principles study, *Physica B* **668**, 415224 (2023).

[21] J. Ishizuka, K. Nogaki, M. Sigrist, and Y. Yanase, Correlation-induced Fermi surface evolution and topological crystalline superconductivity in CeRh₂As₂, *Phys. Rev. B* **110**, L140505 (2024).

[22] Y. Wu, Y. Zhang, S. Ju, Y. Hu, Y. Huang, Y. Zhang, H. Zhang, H. Zheng, G. Yang, E.-O. Eljaouhari, B. Song, N. C. Plumb, F. Steglich, M. Shi, G. Zwicknagl, C. Cao, H. Yuan, and Y. Liu, Fermi surface nesting with heavy quasiparticles in the locally noncentrosymmetric superconductor CeRh₂As₂, *Chinese Phys. Lett.* **41**, 097403 (2024).

[23] H.-T. Ma, P.-F. Tian, D.-L. Guo, X. Ming, X.-J. Zheng, Y. Liu, and H. Li, Phase evolution of Ce-based heavy-fermion superconductors under compression: A combined first-principles and effective-model study, *Phys. Rev. B* **109**, 195164 (2024).

[24] T. Yoshida, M. Sigrist, and Y. Yanase, Pair-density wave states through spin-orbit coupling in multilayer superconductors, *Phys. Rev. B* **86**, 134514 (2012).

[25] D. Möckli and A. Ramires, Superconductivity in disordered locally noncentrosymmetric materials: An application to CeRh₂As₂, *Phys. Rev. B* **104**, 134517 (2021).

[26] E. G. Schertenleib, M. H. Fischer, and M. Sigrist, Unusual *H*-*T* phase diagram of CeRh₂As₂: The role of staggered noncentrosymmetry, *Phys. Rev. Res.* **3**, 023179 (2021).

[27] A. Skurativska, M. Sigrist, and M. H. Fischer, Spin response and topology of a staggered-Rashba superconductor, *Phys. Rev. Res.* **3**, 033133 (2021).

[28] A. Ptok, K. J. Kapcia, P. T. Jochym, J. Lażewski, A. M. Oleś, and P. Piekarz, Electronic and dynamical properties of CeRh₂As₂: Role of Rh₂As₂ layers and expected orbital order, *Phys. Rev. B* **104**, L041109 (2021).

[29] K. Machida, Violation of pauli-clogston limit in the heavy-fermion superconductor CeRh₂As₂: Duality of

itinerant and localized $4f$ electrons, *Phys. Rev. B* **106**, 184509 (2022).

[30] D. C. Cavanagh, T. Shishidou, M. Weinert, P. M. R. Brydon, and D. F. Agterberg, Nonsymmorphic symmetry and field-driven odd-parity pairing in CeRh_2As_2 , *Phys. Rev. B* **105**, L020505 (2022).

[31] D. Möckli, Unconventional singlet-triplet superconductivity, *J. Phys.: Conf. Ser.* **2164**, 012009 (2022).

[32] T. Hazra and P. Coleman, Triplet pairing mechanisms from Hund's-Kondo models: Applications to UTe_2 and CeRh_2As_2 , *Phys. Rev. Lett.* **130**, 136002 (2023).

[33] D. C. Cavanagh, D. F. Agterberg, and P. M. R. Brydon, Pair breaking in superconductors with strong spin-orbit coupling, *Phys. Rev. B* **107**, L060504 (2023).

[34] H. G. Suh, Y. Yu, T. Shishidou, M. Weinert, P. M. R. Brydon, and D. F. Agterberg, Superconductivity of anomalous pseudospin in nonsymmorphic materials, *Phys. Rev. Res.* **5**, 033204 (2023).

[35] K. Nogaki and Y. Yanase, Field-induced superconductivity mediated by odd-parity multipole fluctuation, *Phys. Rev. B* **110**, 184501 (2024).

[36] A. L. Szabó, M. H. Fischer, and M. Sigrist, Effects of nucleation at a first-order transition between two superconducting phases: Application to CeRh_2As_2 , *Phys. Rev. Res.* **6**, 023080 (2024).

[37] A. Amin, H. Wu, T. Shishidou, and D. F. Agterberg, Kramers' degenerate magnetism and superconductivity, *Phys. Rev. B* **109**, 024502 (2024).

[38] A. Minamide and Y. Yanase, Superconducting meron phase in locally noncentrosymmetric superconductors, *Phys. Rev. Lett.* **134**, 026002 (2025).

[39] C. Lee, D. F. Agterberg, and P. M. R. Brydon, Unified picture of superconductivity and magnetism in CeRh_2As_2 , *Phys. Rev. Lett.* **135**, 026003 (2025).

[40] S. Mishra, Y. Liu, E. D. Bauer, F. Ronning, and S. M. Thomas, Anisotropic magnetotransport properties of the heavy-fermion superconductor CeRh_2As_2 , *Phys. Rev. B* **106**, L140502 (2022).

[41] M. Pfeiffer, K. Semeniuk, J. F. Landaeta, R. Borth, C. Geibel, M. Nicklas, M. Brando, S. Khim, and E. Hassinger, Pressure-tuned quantum criticality in the locally noncentrosymmetric superconductor CeRh_2As_2 , *Phys. Rev. Lett.* **133**, 126506 (2024).

[42] G. Chajewski and D. Kaczorowski, Discovery of magnetic phase transitions in heavy-fermion superconductor CeRh_2As_2 , *Phys. Rev. Lett.* **132**, 076504 (2024).

[43] P. Khanenko, J. F. Landaeta, S. Ruet, T. Lühmann, K. Semeniuk, M. Pelly, A. W. Rost, G. Chajewski, D. Kaczorowski, C. Geibel, S. Khim, E. Hassinger, and M. Brando, Phase diagram of CeRh_2As_2 for out-of-plane magnetic field, *Phys. Rev. B* **112**, L060501 (2025).

[44] R. Shiina, H. Shiba, and P. Thalmeier, Magnetic-field effects on quadrupolar ordering in a Γ_8 -quartet system CeB_6 , *J. Phys. Soc. Jpn.* **66**, 1741 (1997).

[45] Y. Kuramoto, H. Kusunose, and A. Kiss, Multipole orders and fluctuations in strongly correlated electron systems, *J. Phys. Soc. Jpn.* **78**, 072001 (2009).

[46] P. Khanenko, D. Hafner, K. Semeniuk, J. Banda, T. Lühmann, F. Bärtl, T. Kotte, J. Wosnitza, G. Zwicknagl, C. Geibel, J. F. Landaeta, S. Khim, E. Hassinger, and M. Brando, Origin of the non-fermi-liquid behavior in CeRh_2As_2 , *Phys. Rev. B* **111**, 045162 (2025).

[47] K. Miyake and A. Tsuruta, A possible scenario for the anomalous temperature dependence of the resistivity and the specific heat of CeRh_2As_2 above the superconducting transition temperature and an origin of the phase transition at $T = T_0$, *J. Phys. Soc. Jpn.* **93**, 074702 (2024).

[48] G. Zwicknagl, Quasi-particles in heavy fermion systems, *Adv. Phys.* **41**, 203 (1992).

[49] D. S. Christovam, M. Ferreira-Carvalho, A. Marino, M. Sundermann, D. Takegami, A. Melendez-Sans, K. D. Tsuei, Z. Hu, S. Rößler, M. Valvidares, M. W. Haverkort, Y. Liu, E. D. Bauer, L. H. Tjeng, G. Zwicknagl, and A. Severing, Spectroscopic evidence of Kondo-induced quasiquartet in CeRh_2As_2 , *Phys. Rev. Lett.* **132**, 046401 (2024).

[50] H. Harima, Hidden-orders of uranium compounds, *SciPost Phys. Proc.* **11**, 006 (2023).

[51] B. Schmidt and P. Thalmeier, Anisotropic magnetic and quadrupolar H - T phase diagram of CeRh_2As_2 , *Phys. Rev. B* **110**, 075154 (2024).

[52] P. Thalmeier, A. Akbari, and B. Schmidt, Thermodynamics, elastic anomalies and excitations in the field induced phases of CeRh_2As_2 , *New J. Phys.* **27**, 033026 (2025).

[53] K. Koepernik and H. Eschrig, Full-potential nonorthogonal local-orbital minimum-basis band-structure scheme, *Phys. Rev. B* **59**, 1743 (1999).

[54] I. Opahle, K. Koepernik, and H. Eschrig, Full-potential band-structure calculation of iron pyrite, *Phys. Rev. B* **60**, 14035 (1999).

[55] H. Eschrig and K. Koepernik, Tight-binding models for the iron-based superconductors, *Phys. Rev. B* **80**, 104503 (2009).

[56] K. Koepernik, O. Janson, Y. Sun, and J. van den Brink, Symmetry-conserving maximally projected Wannier functions, *Phys. Rev. B* **107**, 235135 (2023).

[57] A. Georges, G. Kotliar, W. Krauth, and M. J. Rozenberg, Dynamical mean-field theory of strongly correlated fermion systems and the limit of infinite dimensions, *Rev. Mod. Phys.* **68**, 13 (1996).

[58] G. Kotliar, S. Y. Savrasov, K. Haule, V. S. Oudovenko, O. Parcollet, and C. A. Marianetti, Electronic structure calculations with dynamical mean-field theory, *Rev. Mod. Phys.* **78**, 865 (2006).

[59] P. Delange, S. Biermann, T. Miyake, and L. Pourovskii, Crystal-field splittings in rare-earth-based hard magnets: An ab initio approach, *Phys. Rev. B* **96**, 155132 (2017).

[60] L. V. Pourovskii, J. Boust, R. Ballou, G. G. Eslava, and D. Givord, Higher-order crystal field and rare-earth magnetism in rare-earth- Co_5 intermetallics, *Phys. Rev. B* **101**, 214433 (2020).

[61] V. I. Anisimov, F. Aryasetiawan, and A. I. Lichtenstein, First-principles calculations of the electronic structure and spectra of strongly correlated systems: the LDA + U method, *J. Phys.: Condens. Matter* **9**, 767 (1997).

[62] I. L. M. Locht, Y. O. Kvashnin, D. C. M. Rodrigues, M. Pereiro, A. Bergman, L. Bergqvist, A. I. Lichtenstein, M. I. Katsnelson, A. Delin, A. B. Klautau, B. Johansson, I. Di Marco, and O. Eriksson, Standard model of the rare earths analyzed from the Hubbard I approximation, *Phys. Rev. B* **94**, 085137 (2016).

[63] J. F. Herbst, R. E. Watson, and J. W. Wilkins, Relativistic calculations of $4f$ excitation energies in the rare-earth metals: Further results, *Phys. Rev. B* **17**, 3089 (1978).

[64] J. F. Landaeta, A. M. León, S. Zwickel, T. Lühmann, M. Brando, C. Geibel, E.-O. Eljaouhari, H. Rosner, G. Zwicknagl, E. Hassinger, and S. Khim, Conventional

type-II superconductivity in locally noncentrosymmetric LaRh_2As_2 single crystals, *Phys. Rev. B* **106**, 014506 (2022).

[65] J. Otsuki, K. Yoshimi, H. Shinaoka, and Y. Nomura, Strong-coupling formula for momentum-dependent susceptibilities in dynamical mean-field theory, *Phys. Rev. B* **99**, 165134 (2019).

[66] J. Otsuki, K. Yoshimi, H. Shinaoka, and H. O. Jeschke, Multipolar ordering from dynamical mean field theory with application to CeB_6 , *Phys. Rev. B* **110**, 035104 (2024).

[67] S. Itokazu, A. Kirikoshi, H. O. Jeschke, and J. Otsuki, From localized $4f$ electrons to anisotropic exchange interactions in ferromagnetic CeRh_6Ge_4 , *Commun. Mater.* **6**, 269 (2025).

[68] L. V. Pourovskii, Two-site fluctuations and multipolar intersite exchange interactions in strongly correlated systems, *Phys. Rev. B* **94**, 115117 (2016).

[69] L. V. Pourovskii and S. Khmelevskyi, Quadrupolar superexchange interactions, multipolar order, and magnetic phase transition in UO_2 , *Phys. Rev. B* **99**, 094439 (2019).

[70] H. Kusunose, R. Oiwa, and S. Hayami, Symmetry-adapted modeling for molecules and crystals, *Phys. Rev. B* **107**, 195118 (2023).

[71] S. Hayami and H. Kusunose, Unified description of electronic orderings and cross correlations by complete multipole representation, *J. Phys. Soc. Jpn.* **93**, 072001 (2024).

[72] T. Inui, Y. Tanabe, and Y. Onodera, *Group Theory and Its Applications in Physics*, Springer Series in Solid-State Sciences (Springer Berlin Heidelberg, 2012).

[73] L. D. Landau and E. M. Lifshitz, *Statistical Physics*, 3rd ed. (Butterworth-Heinemann, Oxford, England, 1996).

[74] H. Shiba, O. Sakai, and R. Shiina, Nature of Ce-Ce interaction in CeB_6 and its consequences, *J. Phys. Soc. Jpn.* **68**, 1988 (1999).

[75] T. Yamada and K. Hanzawa, Derivation of RKKY interaction between multipole moments in CeB_6 by the effective wannier model based on the bandstructure calculation, *J. Phys. Soc. Jpn.* **88**, 084703 (2019).

[76] J. M. Perez-Mato, S. V. Gallego, E. S. Tasci, L. Elcoro, G. de la Flor, and M. I. Aroyo, Symmetry-based computational tools for magnetic crystallography, *Annu. Rev. of Mater. Res.* **45**, 217 (2015).

[77] D. B. Litvin, *Magnetic Group Tables: 1-, 2- and 3-dimensional magnetic subperiodic groups and magnetic space groups* (International Union of Crystallography, Chester, England, 2013).

[78] M. Yatsushiro, H. Kusunose, and S. Hayami, Multipole classification in 122 magnetic point groups for unified understanding of multiferroic responses and transport phenomena, *Phys. Rev. B* **104**, 054412 (2021).